Anharmonicity and Disorder in the Black Phases of Cesium Lead Iodide used for Stable Inorganic Perovskite Solar Cells

Arthur Marronnier, Guido Roma, Soline Boyer-Richard, Laurent Pedesseau, Jean-Marc Jancu, Yvan Bonnassieux, Claudine Katan, Constantinos C Stoumpos, Mercouri G Kanatzidis, Jacky Even

Anharmonicity and Disorder in the Black Phases of Cesium Lead Iodide used for Stable Inorganic Perovskite Solar Cells

Arthur Marronnier,*,† Guido Roma,‡ Soline Boyer-Richard,¶ Laurent Pedesseau,¶ Jean-Marc Jancu,¶ Yvan Bonnassieux,† Claudine Katan,§ Constantinos C. Stoumpos,*,‖ Mercouri G. Kanatzidis,‖ and Jacky Even*,¶

†*LPICM, CNRS, Ecole Polytechnique, Université Paris-Saclay, 91128 Palaiseau, France*

‡*DEN - Service de Recherches de Métallurgie Physique, CEA, Université Paris-Saclay, 91191 Gif sur Yvette, France*

¶*Univ Rennes, INSA Rennes, CNRS, Institut FOTON — UMR 6082, F-35000 Rennes, France*

§*Univ Rennes, ENSCR, INSA Rennes, CNRS, ISCR (Institut des Sciences Chimiques de Rennes) – UMR 6226, F-35000 Rennes, France*

‖*Department of Chemistry and Argonne-Northwestern Solar Energy Research (ANSER) Center, Northwestern University, Evanston, Illinois 60208, United States*

E-mail: arthur.marronnier@polytechnique.edu; konstantinos.stoumpos@northwestern.edu; jacky.even@insa-rennes.fr

Abstract

Hybrid organic-inorganic perovskites emerged as a new generation of absorber materials for high-efficiency low-cost solar cells in 2009. Very recently, fully inorganic perovskite quantum dots also led to promising efficiencies, making them a potentially stable and efficient alternative to their hybrid cousins. Currently, the record efficiency is obtained with $CsPbI_3$ whose crystallographical characterization is still limited. Here we show through high resolution in-situ synchrotron XRD measurements that $CsPbI_3$ can be undercooled below its transition temperature and temporarily maintained in its perovskite structure down to room temperature, stabilizing a metastable perovskite polytype (black γ-phase) crucial for photovoltaic applications. Our analysis of the structural phase transitions reveals a highly anisotropic evolution of the individual lattice parameters *versus* temperature. Structural, vibrational and electronic properties of all the experimentally observed black phases are further inspected based on several theoretical approaches. While the black γ-phase is shown to behave harmonically around equilibrium, for the tetragonal phase density functional theory reveals the same anharmonic behavior, with a Brillouin zone-centered double-well instability, as for the cubic phase. Using total energy and vibrational entropy calculations, we highlight the competition between all the low-temperature phases of $CsPbI_3$ (γ, δ, β) and show that avoiding the order-disorder entropy term arising from double-well instabilities is key in order to prevent the formation of the yellow perovskitoid phase. A symmetry-based tight-binding model, validated by self-consistent GW calculations including spin-orbit coupling, affords further insight into their electronic properties, with evidence of Rashba effect for both cubic and tetragonal phases when using the symmetry breaking structures obtained through frozen phonon calculations.

Keywords

inorganic perovskite solar cells, anharmonicity, cesium, phonons, DFT, SXRD, Rashba

The interest of the photovoltaics community for hybrid perovskite solar cells (PSCs) has been growing rapidly since the first demonstration in 2009,[1] mainly because PSCs combine ease and low-cost fabrication of organic electronics with efficiencies which compete with those of traditional sectors, considering the highest certified efficiency of 22.7%.[2] In the race to commercialization, the methylamonium-based perovskite $CH_3NH_3PbI_3$ ($MAPbI_3$ or "MAPI") will probably be outpaced by more stable perovskite structures because of its poor stability.[3] Several strategies are currently being explored, such as mixed cation recipes,[4] layered-perovskites,[5] and nano-structures such as quantum dots.[6] In fact, after Eperon *et al.* found in 2015 a new experimental method in order to maintain $CsPbI_3$ stable in its black phase at room temperature and realized the first working cesium lead iodide solar cell,[7] a cell exceeding 10% efficiency was reported in 2016.[8] It was also shown[9] that adding a small quantity of $EDAPbI_4$ (EDA = ethylenediamine) prevents the formation of the nonperovskite yellow phase of $CsPbI_3$ and leads to a reproducible efficiency of 11.8%. The recent report of a 13.4% efficient cesium lead iodide perovskite quantum dot solar cell[6] has demonstrated that purely inorganic perovskite solar cells have definitively become a stable and efficient alternative to their hybrid cousins. Besides, a four-terminal tandem cell using the formamidinium organic cation along with a small fraction of cesium as well as halogen alloying, in order to be able to tune the band gap, has reached more than 25% efficiency.[10]

It is currently well-known that the crystal structure has a direct impact on device performance and it is thus of crucial importance to have high-quality crystallographic data so as to obtain valuable references for structural characterization of thin films or quantum dots used in those devices. So far, the structure of $CsPbI_3$ has mainly been studied through its similarities with the lead-free perovskite $CsSnI_3$. In fact, the structure of the black orthorhombic γ-phase of $CsSnI_3$ was experimentally measured in 1991,[11] and twenty years later all its crystallographic phases have reached a comprehensive understanding (experimental and theoretical).[1,12–16] For $CsMI_3$ (M=Pb, Sn), four phases are expected:[12,17] cubic (α), tetragonal (β), and two orthorhombic phases (a black γ and a non-perovskite yellow

δ-phase), thus including transitions between perovskite phases and non-perovskite polytypes (perovskitoids)[18] at low temperature. All the phases of $CsSnI_3$ have been thoroughly characterized,[12,19] as well as the room temperature δ-phase of $CsPbI_3$.[17,19,20] More recently, some of us investigated the temperature dependence of $CsPbI_3$'s band gap and how reversible the non-perovskite to perovskite structural transformations at high temperature[21] can be. It was shown that, after heating the samples above 360 °C, the room temperature δ-phase (yellow) converts to the black perovskite α-phase . At variance, during the cooling step, the perovskite structure converts at 260 °C to the β-phase and at 175 °C to the γ-phase; both these phases are black. Only after a few days the yellow δ-phase is obtained again. This work was the first report on the black orthorhombic γ-phase that is crucial in the context of photovoltaics applications.

In addition, vibrational properties of cesium halide perovskites have proven to be a key factor in determining the stability of phases with temperature. In $CsPbCl_3$ the role of phonons in phase transitions was pointed out already in the seventies.[22] Recently, first principles calculations on $CsSnI_3$ revealed soft phonon modes and strong anharmonicity.[23,24] Conversely, in the case of $CsPbI_3$ (and $RbPbI_3$), the role of vibrational properties in determining the phase stability is still under-studied, although large values of Born effective charges hinted towards possible structural instabilities.[25] Very recently, some of us evidenced unexpected anharmonic features in the form of Brillouin zone-centered double-well instability for both the cubic α-phase and the yellow orthorhombic δ-phase of $CsPbI_3$,[26] but due to lack of experimental data on the other phases, our understanding remained incomplete. As for hybrid perovskites, several groups[27,28] revealed small lifetimes for the phonons, a consequence of double-well potential energy profiles at M and R points in the BZ of cubic $CH_3NH_3PbI_3$. These structural effects in hybrid organic-inorganic perovskites, complicated by the rotational motion of the cation, have an influence on the optoelectronic properties. For instance, octahedral tilting has been shown to have a direct impact on the continuum band gap.[29,30] This was further investigated by Yang *et al.*[31] who considered the influence of

temperature on the electronic band structure as well as on the optical absorption threshold of cubic $MAPbI_3$. However, from this and other works[27,32] it seems that the influence of soft phonon modes on the absorption threshold in $MAPbI_3$ can be neglected.

In this paper, we report the detailed experimental structures of the crucial black γ-phase of $CsPbI_3$ at 325K, along with the structures of the α- (645K) and β- (510K) phases, using synchrotron X-ray powder diffraction (SXRD). The temperature-distortion of these three phases is studied. Using DFPT (Density Functional Perturbation Theory) methods similar to our previous work,[26] we investigate the vibrational properties and the energy landscape of both the low-temperature orthorhombic γ-phase and the tetragonal β-phase of $CsPbI_3$. For the tetragonal phase, the instabilities at the Γ point are further studied performing total energy calculations on a path following the soft phonon eigenvectors (frozen phonons method). The energy competition between the low-temperature phases of $CsPbI_3$ is studied using total energy and vibrational entropy calculations. Finally, we used symmetry-based tight-binding modeling and the self-consistent many-body (scGW) approximation to derive the electronic band structure, using our experimental data on the different phases of $CsPbI_3$ and a previously developed tight binding model for hybrid perovskite $MAPbI_3$.[33] We explore the Rashba effect for both cubic and tetragonal phases using the new symmetry-breaking structures revealed by our frozen phonon calculations.

Results and Discussion

Structural distortion of the black phases of $CsPbI_3$

$CsPbI_3$ is one of the earliest known ternary plumbohalides, originally discovered by Møller,[20] having the distinctive characteristic that it adopts a different, "perovskitoid",[18] structure compared to its well-known congeners $CsPbBr_3$ and $CsPbCl_3$ that adopt a regular perovskite structure.[34] Later studies have in fact shown that $CsPbI_3$ can become a perovskite at elevated temperatures (around 310°C),[17] but its structural reconfiguration as it cools

back to room temperature is unknown. We show here that $CsPbI_3$ can be undercooled below its transition temperature and temporarily retain its perovskite structure down to room temperature as shown by high resolution synchrotron X-ray diffraction (figure 1a), using an in-situ experimental setup (figure 1b,1c). The structural analysis confirms the change of the yellow phase (δ-phase) to its black polytype (α-phase) on heating but upon cooling the perovskite does not return to its original yellow phase immediately. Instead, $CsPbI_3$ adopts the metastable perovskite polytype on cooling back to room temperature, revealing a phase transition pathway reminiscent of $CsPbBr_3$,[35,36] $CsSnBr_3$[37,38] and $CsSnI_3$[12,39] where the high symmetry cubic phase (α-phase) distorts initially to a tetragonal phase (β-phase) followed by a further change to the orthorhombic (γ-phase) which persists down to room temperature (figure 2).

The conversion of the δ-$CsPbI_3$ to the α-$CsPbI_3$ involves a dramatic change in the unit cell volume (figures 3a, 3b) which is compensated by a large increase in the thermal parameters of the iodide ions, signaling a very large increase in the dynamic motion of the corner-connected $[PbI_{6/2}]^-$ octahedra. The dynamic motion, which is corroborated by the emergence of stereochemical activity at higher temperature, known as "emphanisis",[40,41] progressively relaxes to less dynamic states (β-$CsPbI_3$, γ-$CsPbI_3$) as the perovskite cools. Quite remarkably, whereas the overall thermal expansion coefficient is positive, the evolution of the individual lattice parameters is highly anisotropic involving a combination of negative and positive thermal expansion coefficients (figure 3c). Initially the crystallographic c-axis expands on cooling in the tetragonal phase regime, followed by a large expansion of the crystallographic b-axis in the orthorhombic phase which is largely compensated by the enormous decrease in the crystallographic a-axis. The competing thermal expansion leads to a crossing of the increasing b-axis and the decreasing c-axis which become equivalent slightly above room temperature. The complex phase transitions in $CsPbI_3$ have also been confirmed by Differential Thermal Analysis (DTA) which supports all the phase changes observed experimentally by XRD.

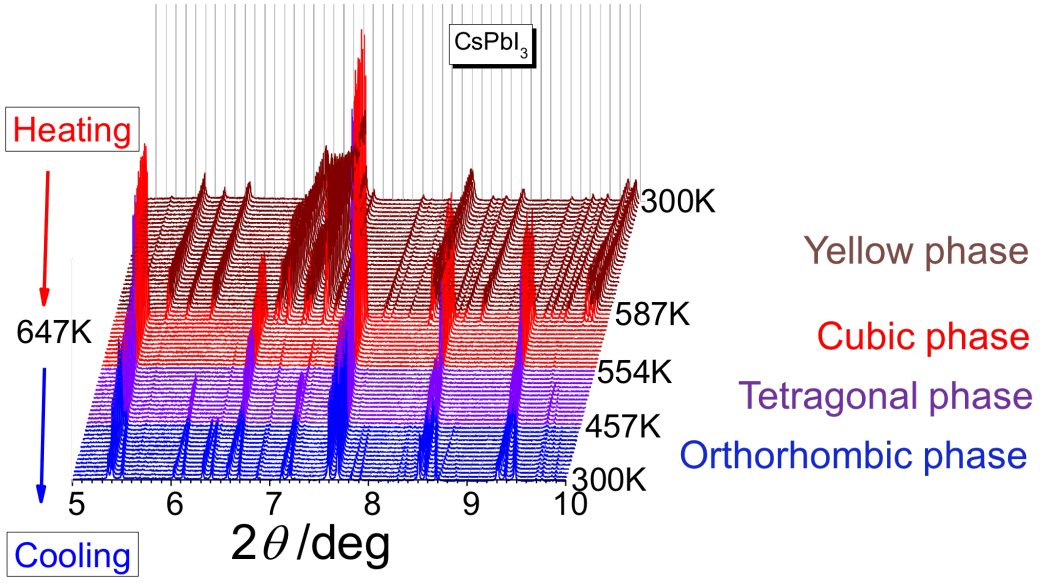

(a)

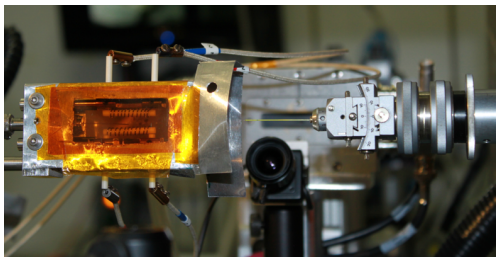

(b)

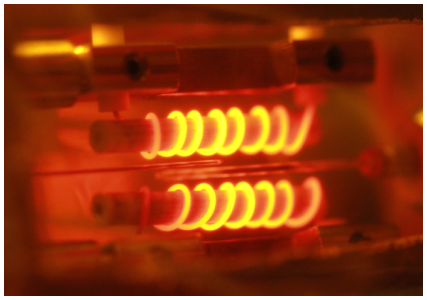

(c)

Figure 1: **Temperature dependent synchrotron XRD (SXRD).** (a) SXRD spectra for $CsPbI_3$. The original yellow phase, converts to the black phase upon heating, but does not return to the original structure upon cooling. (b), (c) The experimental setup used for the *in situ* SXRD measurement of $CsPbI_3$ before and during the experiments. Photos (b) and (c) are courtesy of 11BM of Advanced Photon Source at Argonne National Laboratory.

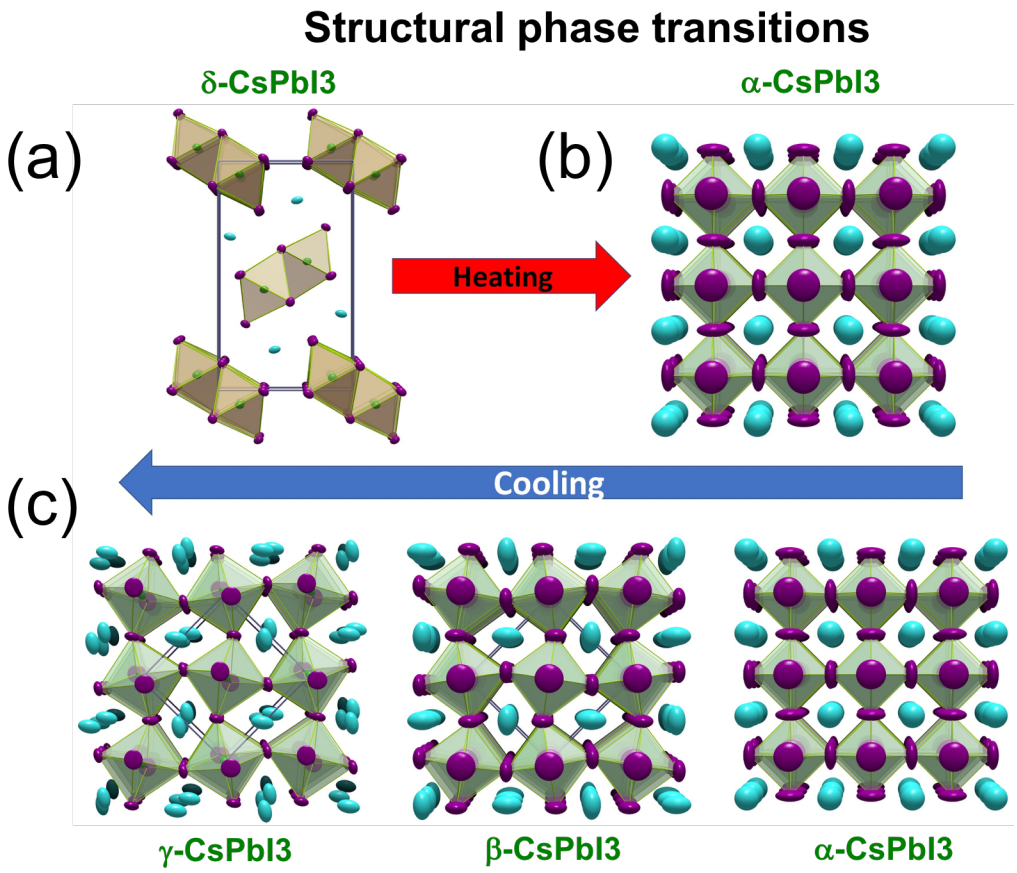

Figure 2: **Structural phase transitions in $CsPbI_3$ *versus* temperature.** (a) The initial yellow perovskitoid phase (δ-$CsPbI_3$, NH_4CdCl_3-type) converts to (b) the black perovskite phase (α-$CsPbI_3$, $CaTiO_3$-type) as the temperature exceeds the transition temperature. (c) Upon cooling, the black perovskite phase is retained and can be undercooled below the transition temperature, where the typical perovskite distortions (tetragonal β-$CsPbI_3$, orthorhombic γ-$CsPbI_3$) can be observed all the way to room temperature. These phases are metastable and transform to the thermodynamic δ-$CsPbI_3$ upon standing.

Vibrational properties and phase competition

In order to get further insight into these black-perovskite phases, we used DFT for structural optimization, which is mandatory to allow inspection of vibrational properties (phonons). We start from the above experimental crystal structures (Figure S4) for the α (645K), β (510K) and γ (325K) phases having, respectively, $Pm\bar{3}m$, $P4/mbm$ and $Pbnm$ space groups. Relaxing the structure from these experimental data sets, we obtain a good agreement on the lattice constants between our XRD experiments (table 1) and our DFT calculations

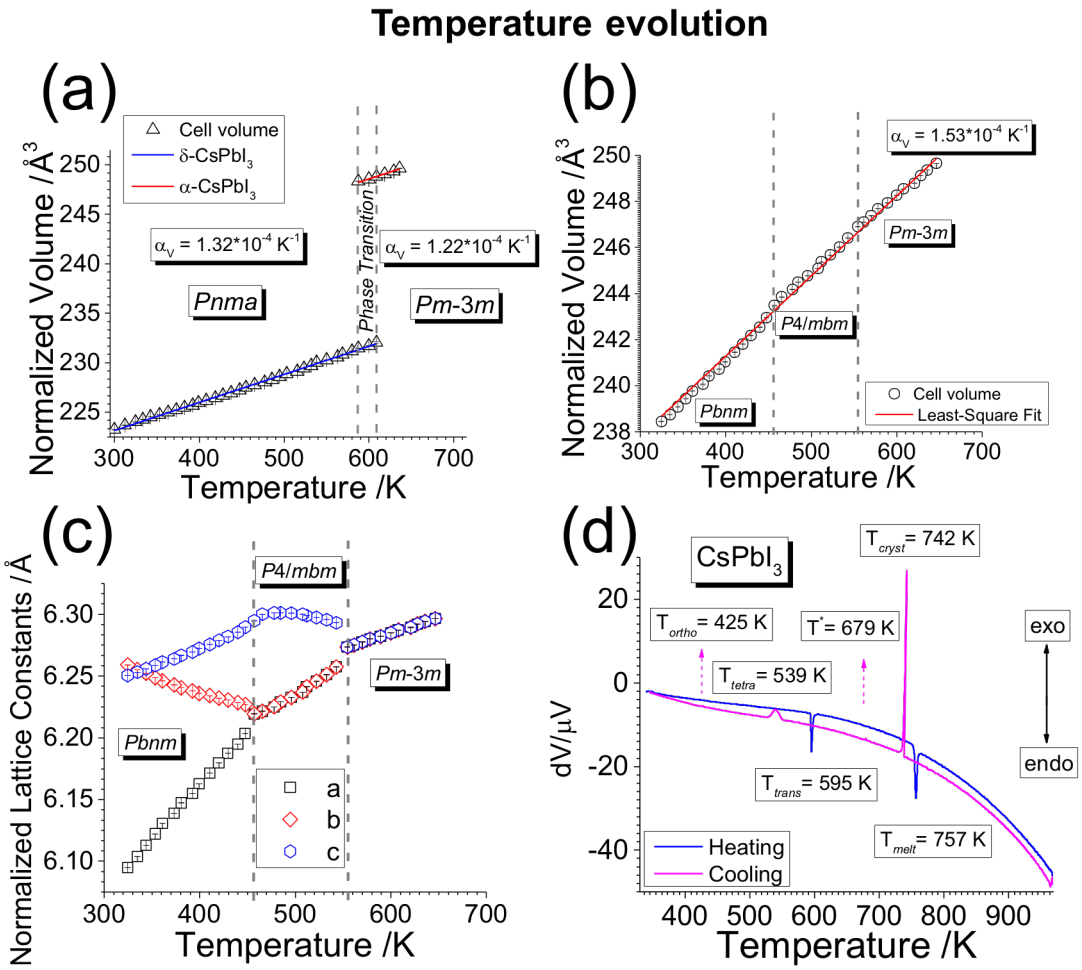

Figure 3: **Temperature evolution of** $CsPbI_3$**.** (a) δ-$CsPbI_3$ ($Pnma$) expands linearly on heating up to the transition temperature at around 600K where the phase transition to α-$CsPbI_3$ ($Pm\bar{3}m$) produces a large increase in the cell volume. (b) On cooling, α-$CsPbI_3$ undergoes successive phase transitions to β-$CsPbI_3$ ($P4/mbm$) and γ-$CsPbI_3$ ($Pbnm$) without converting back to the original δ-$CsPbI_3$ phase. (c) The anisotropic temperature evolution of the $CsPbI_3$ perovskite revealing competitive negative and positive thermal expansion trends among the individual lattice parameters of the low temperature phases. (d) Differential thermal analysis (DTA) is in good agreement with XRD experiments. Legend: T_{melt} = melting point, T_{cryst} = crystallization point, T_{trans} = δ- to α-$CsPbI_3$ transition, T_{tetra} = α- to β-$CsPbI_3$ transition, T_{ortho}= β- to γ-$CsPbI_3$ transition, T^* = Cs_4PbI_6 formation.

(table 2), the latter corresponding to a temperature of 0 K. For instance, the normalized volume at 0 K can be extrapolated from figure 3b and we found 227 $\AA^3$ which is in good agreement with the DFT value obtained for the δ-phase (215 $\AA^3$). We also report in tables 1 and 2 the octahedral tilting with angles β (in-plane) and δ (out-of-plane) calculated as

in Ref. 42, as increased octahedral tilting can be directly traced back to an increase of the continuum band gap in addition to the direct impact of the expansion/contraction of the unit cell parameters. Note that for the orthorhombic phase in the DFT calculations (and later in the phonon calculations) we use the Pnam convention, which is equivalent to Pbnm by a permutation of axes.

Table 1: Normalized lattice constants ($\mathring{A}$) and octahedral tilting angles[42] of the 3 black phases of $CsPbI_3$ from SXRD.

	Pbnm exp. (324.6 K)	*P4/mbm* exp. (511.7 K)	$Pm\overline{3}m$ exp. (646.5 K)
a	6.095	6.241	6.297
b	6.259	6.241	6.297
c	6.250	6.299	6.297
angle β	11°5	8°6	0
angle δ	9°9	0	0

Table 2: Normalized lattice constants ($\mathring{A}$) and octahedral tilting angles[42] of the 3 black phases of $CsPbI_3$ as derived from DFT calculations (at 0 K). We give both the symmetric structures ($\eta = 0$ in figure 4b) and the new equilibrium structures ($\eta \neq 0$ in figure 4b) of the double well found for the *P4/mbm* and $Pm\overline{3}m$ phases.

	Pnam	*P4/mbm* ($\eta = 0$)	*P4/mbm* ($\eta \neq 0$)	$Pm\overline{3}m$ ($\eta = 0$)	$Pm\overline{3}m$ ($\eta \neq 0$)
a	6.335	5.973	5.717	6.149[26]	6.183[26]
b	5.606	5.973	6.222	6.149[26]	6.183[26]
c	6.112	6.273	6.248	6.149[26]	6.183[26]
angle β	0	16°5	10°3 - 22°8	0	2°9 - 3°3
angle δ	0	0	3°7	0	3°6

The orthorhombic, low temperature, γ-phase of $CsPbI_3$ matches the corresponding phase studied experimentally for similar perovskite $CsSnI_3$ in 1991 by Yamada *et al.*[11] who identified it with the *Pbnm* space group symmetry. This is a totally different phase compared to the *Pnma* orthorhombic structure (yellow δ-phase) obtained by Trots[17] and whose phonon

spectrum was already investigated using first-principles calculations.[26] The γ-phase's structure corresponds to a antiferro-distortion of the $Pm\bar{3}m$ perovskite structure as shown previously.[19] Contrary to our previous findings for the α- and δ-phases,[26] the phonon dispersion of the orthorhombic γ-phase of $CsPbI_3$, calculated with DFPT, does not present any imaginary modes at the gamma point (see figure 4d). Furthermore, there are no unstable phonons at the other high symmetry points. This was expected since at low temperature this phase is the most stable perovskite phase.

The phonon dispersions of $CsPbI_3$ in the tetragonal phase (space group $P4/mbm$), with the structure (denoted as "$\eta = 0$" in table 2) optimized starting from our experimental data are shown in figure 4a. The imaginary modes that can be found at different high-symmetry points in the Brillouin zone arise from the instabilities of the tetragonal phase in this zero Kelvin DFT calculation. These modes should be stabilized when including temperature effects *via* vibrational entropy.

The presence of soft modes is less expected at the Γ-point (1 doubly degenerated phonon at -23 cm^{-1}, circled in red), where only acoustic modes should be found. Consistently with earlier findings on the α and δ phases,[26] these instabilities correspond to previous neutron scattering experiments showing very low acoustic phonon density of states at 80°C.[43] Similar results were obtained more recently for $CH_3NH_3PbI_3$[28] and $CH_3NH_3PbBr_3$.[44] These instabilities, especially the one at Γ, were previously reported and analyzed by some of us[26] for both the δ-phase and the α-phase in inorganic $CsPbI_3$. In order to solve this anomaly and to further explore the energy landscape around equilibrium, we use here a similar method of frozen phonons which we do not detail further in this paper.

Using Laudau theory[45] and the adiabatic approximation, the anharmonic energy[22,46] as a function of displacement is given by:

$$U(\eta) = U_0 + \frac{\eta^2}{4}\hbar\omega_{\nu_\Gamma}(\mathbf{q}_\Gamma) + \frac{\eta^4}{24}\Phi_{4,\nu_\Gamma} + O(\eta^6) \quad (1)$$

This model fits well with the results, shown in figure 4. This means that the previous

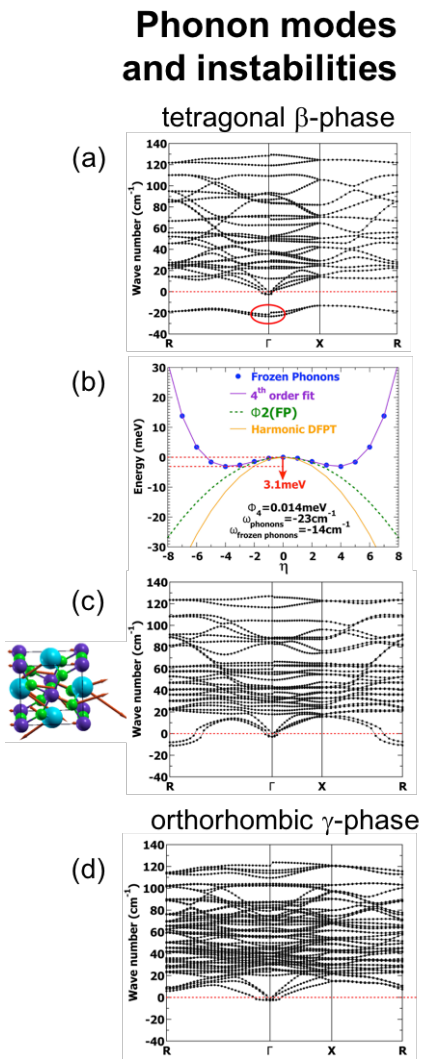

Figure 4: **Phonon modes in $CsPbI_3$.** (a) Phonon modes of the tetragonal β-phase of $CsPbI_3$ in the structure optimized from our experimental data (denoted as "$\eta = 0$" in table 2). Given that the tetragonal structure relaxes to a slightly orthorhombic one when breaking the symmetry (figure c), we use for this figure the same orthorhombic convention for the high-symmetry points of the Brillouin zone as the one used in (c) and (d). (b) Potential energy surface for tetragonal $CsPbI_3$ on a path following the most unstable optical phonon's eigenvector at Γ versus displacement parameter η. A 0.38$\mathring{A}$ 3N dimensional displacement is required to attain the new minimum. $\omega_{frozenphonons}$ and Φ_4 are obtained by fitting equation 1. (c) Phonon modes of tetragonal $CsPbI_3$ at the true equilibrium structure (slightly orthorhombic) obtained through geometry optimization of the symmetry-broken structure (denoted as "$\eta \neq 0$" in table 2). The imaginary modes at Γ were eliminated thanks to tight convergence thresholds and the frozen phonon method. (d) Phonon modes of the orthorhombic γ-phase of $CsPbI_3$ in the structure optimized from our experimental data (see table 2).

structure was not the proper equilibrium state and that the tetragonal phase of $CsPbI_3$ behaves anharmonically around equibrium. The structure will thus oscillate between the two minima and through this very weak energy barrier (3.1 meV). In order to estimate the frequency of these oscillations, one can write:

$$\tau = \tau_0 e^{\frac{E}{k_B T}} \tag{2}$$

for an energy barrier E (and the Boltzmann constant k_B). Assuming for τ_0 the lowest optical phonon frequency ($\omega \approx 23$ cm^{-1}), one finds a typical oscillation time of $0.4 \cdot 10^{-12}$ s at room temperature. After relaxation from the minimum structure obtained by fitting the 4th order model, the energy barrier increases to 8.1 meV. This leads to the new equilibrium structure denoted as "$\eta \neq 0$".

After relaxing from the new symmetry breaking equilibrium positions ($\eta \neq 0$), we could totally eliminate the soft modes at Γ (see figure 4c). To conclude, for the tetragonal phase of $CsPbI_3$ the imaginary modes at Γ were eliminated thanks to both tight convergence thresholds and the frozen phonon method. As a result, this anharmonic phonon at Γ will not condense at low temperatures and will not yield one of the orthorhombic phases whereas the remaining instabilities at the R point correspond to phonon modes which condense at lower temperatures to transition to the orthorhombic black γ-phase.[21,43]

To summarize our comprehensive vibrational study, we have shown here and in Ref. 26 that $CsPbI_3$ presents this anharmonic feature in three out of four phases, at variance with $MAPbI_3$ for which instabilities at the center of the BZ were not found.

Next, we briefly investigate the phase competition and vibrational entropy of the low temperature phases. Table 3 summarizes the total energies of the two different orthorhombic phases of $CsPbI_3$ along with that computed for the tetragonal β-phase. For each phase, we report here the lowest energy obtained by DFT optimization, which means using the symmetry breaking structures for the δ- and β-phases ($\eta \neq 0$).

Table 3: Total energies (U) and free energies (F) of $CsPbI_3$ phases, given per formula unit of 5 atoms.

Phase	Experimental Temperature (K)	U (meV)	F at 400 K (meV)
δ	325	34[26]	88.5
γ	450	0	0
β	510	54	

We find that the γ-phase has a lower total energy than the δ-phase, contrary to what one would expect given their respective temperature of stability. We carefully checked that this conclusion is not changed when using PBE or even HSE exchange-correlation instead of LDA, or when spin orbit coupling is taken into account (see Supplementary Information). Given the structural instabilities of these structures, especially for the δ-phase,[26] one can anticipate relatively high values for the vibrational entropies, potentially reversing this order for the free energy $F = U - TS$. We calculated the free energy F by including the $-TS_{vib}$ term (quasi-harmonic approximation[47]). This method, using the phonon density of states, cannot be straightforwardly applied[23] when unstable phonon modes are present, and can thus be used only for low-temperature orthorhombic phases, once their unstable modes at Γ have been removed (see computational methods for technical details).

The results show that taking into account the vibrational entropy does not change the conclusion: the γ-phase is calculated to have a lower energy than the δ-phase (table 3). This might be due to the fact the δ-phase could actually be further stabilized through an additional order-disorder ΔS stochastic entropy term[48] associated to the structural instabilities (and related to the fourth-order term in equation 1 that we reported for this phase). This term naturally does not apply to the more stable γ-phase.

We think that avoiding the disorder of the non-perovskite phase is key in order to keep $CsPbI_3$ in its stable black phases. In a very recent paper,[9] Zhang *et al.* noticed that the stabilization of α-$CsPbI_3$ is accompanied by a significant reduction in grain size. In light of our findings on the ferroelectric disorder of the δ-phase,[26] the reduced grain size could

prevent the perovskite from forming very small ferroelectric domains and allow it to remain in its ordered black phases.

Electronic properties of the black perovskite phases

We further use the aforementioned XRD and DFT-optimized structures for the different perovskite phases of $CsPbI_3$ to investigate their electronic properties. To this end we employ both semi-empirical and state-of-the-art many-body DFT techniques (see computational section for details). To model non-cubic phases of $CsPbI_3$, we customized the sp^3 tight-binding (TB) model recently developed for the cubic phase of $MAPbI_3$,[33] considering a simple d^{-2} Harrison law[49] to handle bond length variations, along with the matrix elements as given by Slater and Koster.[50] Given the very limited experimental data available for the black phases of $CsPbI_3$, we used the TB parameters reported previously and optimized for $MAPbI_3$.[33]

The electronic band structures computed with the TB model using the experimental crystallographic data recorded for the α (645K), β (510K) and γ (325K) phases of $CsPbI_3$ are shown in figure 5a, 5b and 5c, respectively. All electronic band gaps are direct and corresponding values are summarized in table 4. For the cubic α-phase, the computed band gap (1.6 eV) agrees nicely with the experimental one (1.7 eV).[7,51] As expected, because of band folding[52] the band gap of $CsPbI_3$ shifts from the R point of the Brillouin zone in the cubic α-phase to Z and Γ for the β and γ-phases, respectively. The electronic band gap undergoes a progressive increase when going from the cubic phase to the more distorted β- and γ- phases. This increase is a direct consequence of the lead-iodide octahedra rotations that stabilizes the top of the valence band (VBM) and destabilizes the bottom of the conduction band (CBM) due to, respectively, anti-bonding and bonding character of the orbital overlaps.[52]

Given the limited experimental data, we also performed calculations at a relevant level of theory required to assess bandgaps, namely using the quasiparticle self-consistent GW theory

(scGW) along with spin-orbit coupling (SOC).[53,54] The agreement with the TB model is fairly good (table 4 and figure 5a/b/c), particularly because the parameters of our TB model have not been refined to match any experimental data nor those computed at the scGW+SOC level. The latter confirm the progressive decrease of the bandgap from the γ-phase to the α-phase. These predictions clearly prompt further detailed experimental investigation of all three perovskite black phases.

Table 4: Comparison of electronic band gaps obtained within the TB model and from scGW calculations including SOC for the experimental determined crystal structures (figure 2c).

Phase	E_G (eV) TB	E_G (eV) scGW+SOC	E_G (eV) exp.
γ	2.25	2.53	
β	1.83	1.89	
α	1.61	1.48	1.73[7,51]

Next, we further use our TB model to investigate the electronic properties of the DFT optimized crystal structures of $CsPbI_3$ (table 2). Corresponding electronic band structures are shown in figure 5d and 5e and bandgaps are summarized in table 5. Overall, for the high symmetry structures ($\eta = 0$), the computed band structures reveal the very same features as those obtained for the experimental crystal structures (figure 5). The bandgap of the cubic $Pm\overline{3}m$ structure is significantly reduced as a result of the smaller unit cell parameter (table 5). For the low-symmetry structures ($\eta \neq 0$) band gaps of both the cubic and tetragonal structures undergo a significant increase consistent with octahedral distortions (vide supra). More, the energy minima are shifted away from the high symmetry points of the Brillouin zone (R and Z for the α and β phases, respectively) due to the Rashba effect that lifts the spin degeneracy.[53]

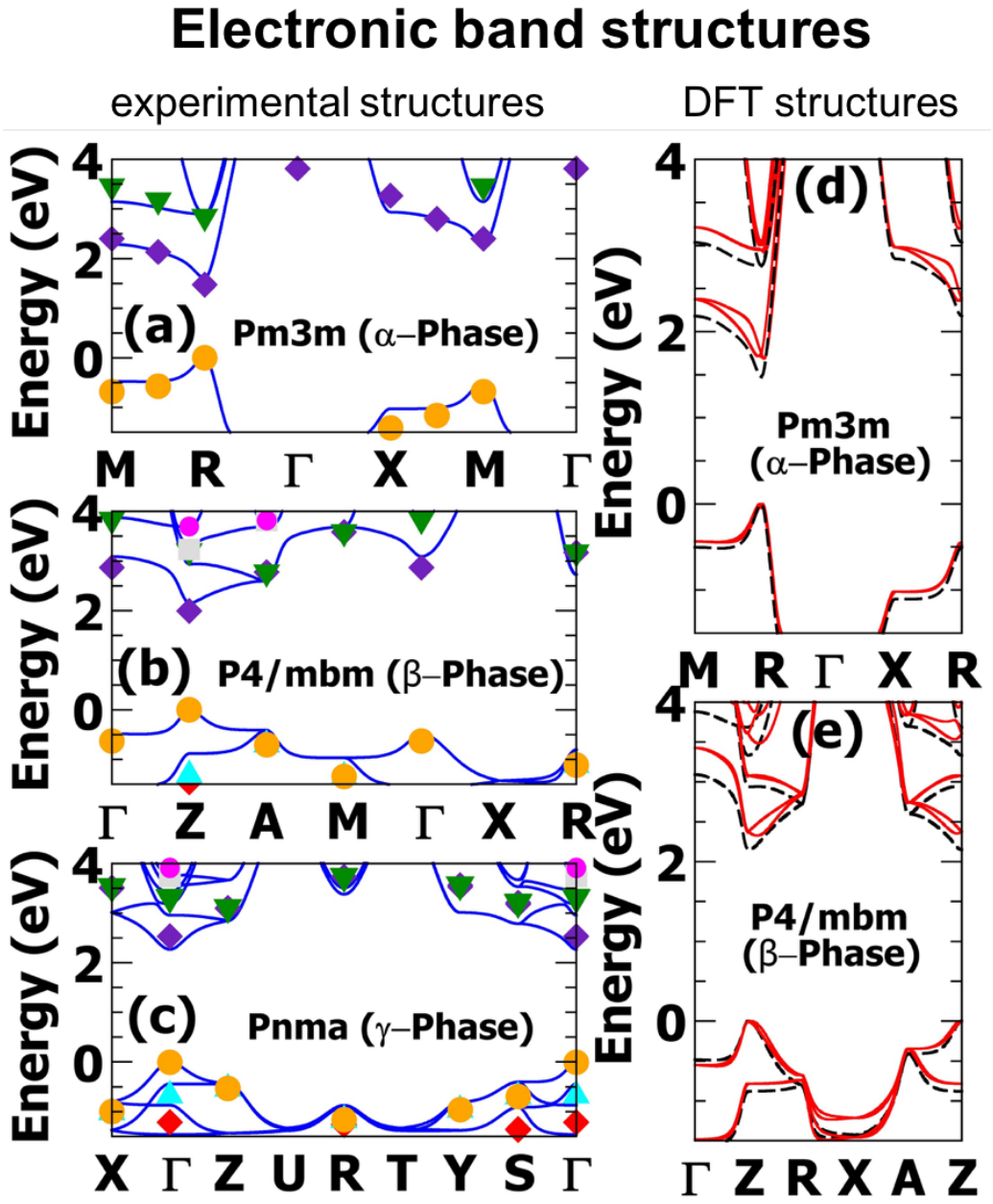

Figure 5: **Electronic band structures.** (a), (b) and (c) Computed electronic band structures using the TB model (full lines) and at the scGW+SOC level of theory (symbols) for the experimentally determined crystal structures (figure 2c). (d) and (e) Electronic band structures calculated from the TB method for the DFT optimized structures (d) cubic α-phase and (e) tetragonal β-phase. Dashed lines correspond to the symmetric structures ($\eta = 0$) whereas straight lines correspond to the new equilibrium structures ($\eta \neq 0$).

Table 5: Data relevant to the Rashba effect: band gap energies for the DFT optimized structures of the cubic α- and tetragonal β-phases. $\eta = 0$ and $\eta \neq 0$ (figure 4b) correspond to the symmetric and new equilibrium structures, respectively. k_{minCB} indicates the position in reciprocal space of the conduction band minimum. ΔE_C is the energy shift between R-point for the α-phase (Z point for the β-phase) and the new conduction band minimum.

Phase	E_G (eV) $\eta = 0$	E_G (eV) $\eta \neq 0$	k_{minCB} $(\frac{\pi}{a}, \frac{\pi}{b}, \frac{\pi}{c})$	ΔE_C (eV)
β	2.15	2.38	(0.166,0,1)	0.05
α	1.47	1.75	$0.963(1, 1, 1)$	0.06

Thus, these results strongly support the hypothesis of dynamical Rashba effect in $CsPbI_3$. They also demonstrate that it is an intrinsic property of the inorganic lattice, even though its strength might be influenced by the nature of the organic cations such as MA or FA.

Concluding Remarks

Using high resolution synchrotron XRD measurements, we showed that $CsPbI_3$ can be undercooled below its transition temperature and temporarily retain its perovskite structure down to room temperature, stabilizing a metastable perovskite polytype (black γ-phase). Our detailed study of the temperature distortion revealed complex phase transitions with a highly anistropic evolution of the individual lattice parameters and even a crossing of the b-axis and c-axis in the *Pbnm* phase. Our ab-initio vibrational calculations have shown that out of the three black phases of $CsPbI_3$, the only phase that presents a harmonic energy landscape around equilibrium is the orthorhombic γ-phase. Avoiding the anharmonic order-disorder entropy term of the non perovskite δ-phase is key in order to keep $CsPbI_3$ in its black phase at room temperature. As for the new tetragonal β-phase, we evidenced unexpected anharmonic effects in the form of a Brillouin zone-centered double-well. This instability could affect in particular the static dielectric constant through the coupling between phonons and the electric field in these materials.[55] In addition, the perovskite oscillations through the double well could be at the origin of the dynamical Rashba effect and the ferroelectricity forseen in halide perovskites.[53] In fact, we evidenced this Rashba effect for the cubic and

tetragonal phase and studied the electronic structure of all three black phases of $CsPbI_3$ combining tight-binding modeling and self-consistent GW calculations in the framework of many body perturbation theory.

Methods

Synthesis

PbO (100 mmol, 22.32 g) was dissolved in 100 ml of 57% aqueous HI. Cs_2CO_3 (50 mmol, 16.29 g) was dissolved in 100 ml of 57% aqueous HI. A yellow solid is obtained from the mixture of CsI and PbO solutions, leaving an essentially colorless supernatant liquid (usually pale yellow because of the presence of dissolved I_2; colorless starting HI should give a practically colorless supernatant). The addition was done slowly, under constant stirring at the initial steps to avoid local concentration of CsI. The mixture was left to cool down to ambient temperature and immediately filtered through a fritted-dish funnel under vacuum. The solid was washed with 5% aqueous HI (5 parts of water/one part of concentrated HI) followed by methanol and left for overnight drying. The solid was further dried in an oven at about 70°C in air. The yield is 72g (around 100%).

An amount of 36 mg (0.05 mmol) of $CsPbI_3$ were mixed with 57 mg (0.95 mmol) of fused SiO_2 and transferred into a mortar which were thoroughly ground into a homogeneous pale yellow powder. The resulting powder was transferred in a 0.5 mm OD fused SiO_2 capillary, filling it to around 2/3 of its length. Neat fused SiO_2 was added on top to facilitate sealing. The capillary was transferred into a vacuum line and flame sealed through the neat SiO_2 at 10^{-4} mbar. For measuring, the capillary was placed into a brass pin sample holder base, held in place by fast drying epoxy, mounted on the goniometer and measured under the following conditions.

High-resolution temperature-dependent X-ray diffraction

High resolution synchrotron powder diffraction experiments were performed at the beamline 11-BM of the Advanced Photon Source (APS), Argonne Nat. Lab.. An average wavelength of $\lambda = 0.413906\mathring{A}$ was used.[56]

A home-made resistive heater device was used to control the temperature of the samples over the range 300-650 K (see figure 1b). The temperature was ramped at a rate of 2.5°K/min and diffraction patterns were recorded every 4 min covering a temperature window of around 10°K/pattern. A thermocouple, protected by a fused SiO_2 sheath, was used to measure the temperature close to the bottom of the sample capillary, from were the data were collected (see figure 1c). The diffractometer was controlled using the EPICS code.[57]

Powder pattern refinements

The powdered patterns were refined using the cyclic refinement function of Jana2006.[58] The initial room temperature pattern was refined using a pseudo-Voigt peak shape model with 20 Legendre polynomial terms used to model the background. The atomic coordinates of the known structure of δ-$CsPbI_3$ were used to initiate the Rietveld refinement with all atoms refining anisotropically. The higher temperature patterns were refined in an automated manner with the initial guesses for each pattern being provided by the preceding one. Upon each phase transition, where the fitting quality decreased significantly, a new initial structural refinement was made manually and the cyclic refinement was repeated until the next phase transition. The initial guesses for the space groups and the atomic positions of α-$CsPbI_3$, β-$CsPbI_3$ and γ-$CsPbI_3$, were found based on screening through the most common perovskite tilting modes.[59] The detailed refinement data is given in the Supplementary Information file.

Density functional theory for vibrational properties study

Electronic-structure calculations were performed within the Density-Functional Theory (DFT)[60,61] framework, as implemented in the Quantum Espresso code.[62] The vibrational properties were studied using the Local Density Approximation (LDA) and plane waves with a cutoff of 70 Ry. The details of the pseudopotentials that we used here, both the scalar relativistic ones and the fully relativistic used to check the influence of spin-orbit coupling, have been described in Ref. 26. Additional calculations to test the effect of the exchange correlation functionals, using PBE and HSE, are described in the Supporting Information. The following Monkhorst-Pack meshes[63] (centered on Γ) were used to describe the various phases: δ-$CsPbI_3$: 10×5×3, α-$CsPbI_3$: 8×8×8, β-$CsPbI_3$: 7×5×5 and γ-$CsPbI_3$: 6×6×4.

We used Density-Functional Perturbation Theory[47] (DFPT) to compute the phonon spectra, as implemented in the Quantum Espresso code.[62] Born effective charges and high-frequency dielectric tensors were computed with linear response theory and gave us access to the long range contributions to the dynamical matrices. A resolution of 5 **q**-points/$\mathring{A}^{-1}$ was chosen for the phonon spectra. To remove spurious phonon modes, we used strict convergence thresholds of $10^{-4} Ry/bohr$ (forces) and 10^{-14} (phonon self-consistency).

The vibrational entropy was estimated for the δ and γ-phases by adding a temperature dependent term to the free energy (quasi-harmonic approximation[47]). The phonon density of states was calculated from the dynamical matrices obtained by DFPT. We neglect thermal expansion, *i.e.*, the phonon frequencies used for the calculation of the vibrational entropy are computed once for all at the zero temperature ground state. The densities of states are shown in figure S6, the corresponding vibrational entropies used for the free energies for the two phases are shown in figure S7. The free energy of γ-phase is always lower than that of the δ-phase.

Many-body perturbation theory for electronic properties (scGW)

DFT calculations, as a starting point for perturbation theory, are performed using the plane-wave projector augmented wave (PAW) implementation available in the VASP software.[64–66] The generalized gradient approximation (GGA-PBE) is used for the exchange-correlation functional.[67,68] The spin-orbit coupling (SOC), mandatory for achieving relevant electronic structure calculations on lead-based perovskites,[52–54] is used as implemented in the VASP code and detailed in Ref. 69. To avoid the underestimation of the electronic band gaps of semi-local DFT with SOC,[52–54] we used quasiparticle self-consistent GW theory[70,71] (scGW) as implemented in the VASP code.[72–74] We used the GGA-PBE relativistic pseudopotentials available in VASP with Cs $[5s^2 5p^6 6s^1]$, Pb $[6s^2 6p^2 5d^{10}]$ and I $[5s^2 5p^5]$. A plane-wave basis set with an energy cut-off of 500 eV is used to expand the electronic wave-functions. The reciprocal space integration is performed over a 2×2×2, 2×2×2 and 4×4×4 Monkhorst-Pack grid[75] for the γ, β and α phases respectively. To reach energy convergence we imposed a tolerance factor of5.10^{-7} eV on the residual potential.

Tight binding model

The sp^3 TB model presented here has been adapted from the one recently developed for the hybrid organic perovskites $MAPbI_3$ in its cubic phase.[33] It is based on a set of 16 basis functions, when spin orbit coupling (SOC) is disregarded, and 32 basis functions when SOC is included. For a cubic AMX_3 halide perovskite, it consists in one s and three p orbitals for the M atom, and the same holds for X atoms. No basis function is needed for the A cation and the model includes nearest neighbor interactions between M and X atoms. The nine parameters to consider (without SOC) are: (i) four matrix elements related to M and X atoms: E_{sM}, E_{pM}, E_{sX} and E_{pX} and (ii) five matrix elements referring to the atomic overlap integrals: V_{ss}, V_{sMpX}, V_{pMsX}, $V_{pp\sigma}$, $V_{pp\pi}$. With SOC, the degenerate p states split into $J = 1/2$ and $3/2$ bands and this splitting is taken into account both for the metal (Δ_{soM}) and halogens (Δ_{soX}). To model the perovskite black phases of $CsPbI_3$, we used

the parameters determined for $MAPbI_3$[33] without further refinement. To address the non-cubic structures having different Metal-Halogen bond lengths, we adapted this TB model considering the expression for the matrix elements reported in the seminal work by Slater and Koster[50] and an additionnal d^{-2} Harrison law,[49] without the need of any additional parameter (for instance, no adjustable prefactor).

Associated Content

The authors declare no competing financial interest.

Acknowledgement

Arthur Marronnier's PhD project is funded by the Graduate School of École des Ponts ParisTech and the French Department of Energy (MTES). HPC resources of TGCC and CINES were used through allocation 2017090642 and x20170906724 GENCI projects. The work at FOTON and ISCR was funded by the European Union's Horizon 2020 program, through a FET Open research and innovation action under the grant agreement No 687008. This work was supported by the U.S. Department of Energy, Office of Science, Basic Energy Sciences under award number DE-SC-0012541 (sample synthesis, X-ray synchrotron, radiation and structural analysis). Use of the Advanced Photon Source at Argonne National Laboratory was supported by the U. S. Department of Energy, Office of Science, Office of Basic Energy Sciences, under Contract No. DE-AC02-06CH11357. The authors would also like to thank A. Garcia Barker for her editing and proofreading contributions.

Supporting Information Available

We provide in the supporting information:

- Additional information about the temperature-dependent XRD measurements (refined patterns of mixed phases)
- Detailed structures and cif files
- A study of the influence of SOC on the energy landscape
- Results on the phase competition when considering alternative exchange-correlation functionals (PBE, HSE) and SOC
- Details on the vibrational entropies

References

1. Kojima, A.; Teshima, K.; Shirai, Y.; Miyasaka, T. Organometal Halide Perovskites as Visible-Light Sensitizers for Photovoltaic Cells. *J. Am. Chem. Soc.* **2009**, *131*, 6050–6051.
2. Best research-cell efficiencies. `https://www.nrel.gov/pv/assets/images/efficiency-chart.png`, Accessed: 2017-11-7.
3. Wang, D.; Wright, M.; Elumalai, N. K.; Uddin, A. Stability of Perovskite Solar Cells. *Sol. Energy Mater. Sol. Cells* **2016**, *147*, 255–275.
4. Saliba, M.; Matsui, T.; Seo, J.-Y.; Domanski, K.; Correa-Baena, J.-P.; Nazeeruddin, M. K.; Zakeeruddin, S. M.; Tress, W.; Abate, A.; Hagfeldt, A.; Grätzel, M. Cesium-containing Triple Cation Perovskite Solar Cells: Improved Stability, Reproducibility and High Efficiency. *Energy Environ. Sci.* **2016**, *9*, 1989–1997.
5. Tsai, H.; Nie, W.; Blancon, J.-C.; Stoumpos, C. C.; Asadpour, R.; Harutyunyan, B.; Neukirch, A. J.; Verduzco, R.; Crochet, J. J.; Tretiak, S.; Pedesseau, L.; Even, J.;

Alam, M. A.; Gupta, G.; Lou, J.; Ajayan, P. M.; Bedzyk, M. J.; Kanatzidis, M. G.; Mohite, A. D. High-efficiency Two-dimensional Ruddlesden–Popper Perovskite Solar Cells. *Nature* **2016**, *536*, 312–316.

6. Sanehira, E. M.; Marshall, A. R.; Christians, J. A.; Harvey, S. P.; Ciesielski, P. N.; Wheeler, L. M.; Schulz, P.; Lin, L. Y.; Beard, M. C.; Luther, J. M. Enhanced Mobility $CsPbI_3$ Quantum Dot Arrays for Record-efficiency, High-voltage Photovoltaic Cells. *Sci. Adv.* **2017**, *3*.

7. Eperon, G. E.; Paterno, G. M.; Sutton, R. J.; Zampetti, A.; Haghighirad, A. A.; Cacialli, F.; Snaith, H. J. Inorganic Caesium Lead Iodide Perovskite Solar Cells. *J. Mater. Chem. A* **2015**, *3*, 19688–19695.

8. Swarnkar, A.; Marshall, A. R.; Sanehira, E. M.; Chernomordik, B. D.; Moore, D. T.; Christians, J. A.; Chakrabarti, T.; Luther, J. M. Quantum Dot–induced Phase Stabilization of α-$CsPbI_3$ Perovskite for High-efficiency Photovoltaics. *Science* **2016**, *354*, 92–95.

9. Zhang, T.; Dar, M. I.; Li, G.; Xu, F.; Guo, N.; Grätzel, M.; Zhao, Y. Bication Lead Iodide 2D Perovskite Component to Stabilize Inorganic α-$CsPbI_3$ Perovskite Phase for High-efficiency Solar Cells. *Sci. Adv.* **2017**, *3*.

10. McMeekin, D. P.; Sadoughi, G.; Rehman, W.; Eperon, G. E.; Saliba, M.; Hörantner, M. T.; Haghighirad, A.; Sakai, N.; Korte, L.; Rech, B.; Johnston, M. B.; Herz, L. M.; Snaith, H. J. A Mixed-cation Lead Mixed-halide Perovskite Absorber for Tandem Solar Cells. *Science* **2016**, *351*, 151–155.

11. Yamada, K.; Funabiki, S.; Horimoto, H.; Matsui, T.; Okuda, T.; Ichiba, S. Structural Phase Transitions of the Polymorphs of $CsSnI_3$ by means of Rietveld Analysis of the X-Ray Diffraction. *Chem. Lett.* **1991**, 801–804.

12. Chung, I.; Song, J.-H.; Im, J.; Androulakis, J.; Malliakas, C. D.; Li, H.; Freeman, A. J.; Kenney, J. T.; Kanatzidis, M. G. $CsSnI_3$: Semiconductor or Metal? High Electrical Conductivity and Strong Near-infrared Photoluminescence from a Single Material. High Hole Mobility and Phase-transitions. *J. Am. Chem. Soc.* **2012**, *134*, 8579–8587.

13. Im, J.-H.; Lee, C.-R.; Lee, J.-W.; Park, S.-W.; Park, N.-G. 6.5% Efficient Perovskite Quantum-dot-Sensitized Solar Cell. *Nanoscale* **2011**, *3*, 4088–4093.

14. Chung, I.; Lee, B.; He, J.; Chang, R. P.; Kanatzidis, M. G. All-solid-state Dye-sensitized Solar Cells with High Efficiency. *Nature* **2012**, *485*, 486.

15. Etgar, L.; Gao, P.; Xue, Z.; Peng, Q.; Chandiran, A. K.; Liu, B.; Nazeeruddin, M. K.; Grátzel, M. Mesoscopic $CH_3NH_3PbI_3/TiO_2$ Heterojunction Solar Cells. *J. Am. Chem. Soc.* **2012**, *134*, 17396–17399.

16. Lee, M. M.; Teuscher, J.; Miyasaka, T.; Murakami, T. N.; Snaith, H. J. Efficient Hybrid Solar Cells based on Meso-superstructured Organometal Halide Perovskites. *Science* **2012**, *338*, 643–647.

17. Trots, D.; Myagkota, S. High-temperature Structural Evolution of Caesium and Rubidium Triiodoplumbates. *J. Phys. Chem. Solids* **2008**, *69*, 2520 – 2526.

18. Stoumpos, C. C.; Mao, L.; Malliakas, C. D.; Kanatzidis, M. G. Structure–Band Gap Relationships in Hexagonal Polytypes and Low-Dimensional Structures of Hybrid Tin Iodide Perovskites. *Inorg. Chem.* **2017**, *56*, 56–73.

19. Stoumpos, C. C.; Malliakas, C. D.; Kanatzidis, M. G. Semiconducting Tin and Lead Iodide Perovskites with Organic Cations: Phase Transitions, High Mobilities, and Near-Infrared Photoluminescent Properties. *Inorg. Chem.* **2013**, *52*, 9019–9038.

20. Møller, C. K. The Structure of Caesium Plumbo Iodide $CsPbI_3$. *Mat. Fys. Medd. Dan. Vid. Sels.* **1959**, *32, No 1*.

21. Stoumpos, C. C.; Kanatzidis, M. G. The Renaissance of Halide Perovskites and Their Evolution as Emerging Semiconductors. *Acc. Chem. Res.* **2015**, *48*, 2791–2802.

22. Fujii, Y.; Hoshino, S.; Yamada, Y.; Shirane, G. Neutron-scattering Study on Phase Transitions of $CsPbCl_3$. *Phys. Rev. B* **1974**, *9*, 4549–4559.

23. Lora da Silva, E.; Skelton, J. M.; Parker, S. C.; Walsh, A. Phase Stability and Transformations in the Halide Perovskite $CsSnI_3$. *Phys. Rev. B* **2015**, *91*, 144107.

24. Patrick, C. E.; Jacobsen, K. W.; Thygesen, K. S. Anharmonic Stabilization and Band Gap Renormalization in the Perovskite $CsSnI_3$. *Phys. Rev. B* **2015**, *92*, 201205.

25. Brgoch, J.; Lehner, A. J.; Chabinyc, M.; Seshadri, R. Ab Initio Calculations of Band Gaps and Absolute Band Positions of Polymorphs of $RbPbI_3$ and $CsPbI_3$: Implications for Main-Group Halide Perovskite Photovoltaics. *J. Phys. Chem. C* **2014**, *118*, 27721–27727.

26. Marronnier, A.; Lee, H.; Geffroy, B.; Even, J.; Bonnassieux, Y.; Roma, G. Structural Instabilities Related to Highly Anharmonic Phonons in Halide Perovskites. *J. Phys. Chem. Lett.* **2017**, *8*, 2659–2665.

27. Whalley, L. D.; Skelton, J. M.; Frost, J. M.; Walsh, A. Phonon Anharmonicity, Lifetimes, and Thermal Transport in $CH_3NH_3PbI_3$ from Many-body Perturbation Theory. *Phys. Rev. B* **2016**, *94*, 220301.

28. Beecher, A. N.; Semonin, O. E.; Skelton, J. M.; Frost, J. M.; Terban, M. W.; Zhai, H.; Alatas, A.; Owen, J. S.; Walsh, A.; Billinge, S. J. L. Direct Observation of Dynamic Symmetry Breaking above Room Temperature in Methylammonium Lead Iodide Perovskite. *ACS Energy Lett.* **2016**, *1*, 880–887.

29. Amat, A.; Mosconi, E.; Ronca, E.; Quarti, C.; Umari, P.; Nazeeruddin, M. K.; Grätzel, M.; De Angelis, F. Cation-Induced Band-Gap Tuning in Organohalide Per-

ovskites: Interplay of Spin–Orbit Coupling and Octahedra Tilting. *Nano Lett.* **2014**, *14*, 3608–3616.

30. Filip, M.; Eperon, G.; J. Snaith, H.; Giustino, F. Steric Engineering of Metal-halide Perovskites with Tunable Optical Band Gaps. *Nat. Commun.* **2014**, *5*.

31. Yang, J.-Y.; Hu, M. Temperature Induced Large Broadening and Blueshift in the Electronic Band Structure and Optical Absorption of Methylammonium Lead Iodide Perovskite. *J. Phys. Chem. Lett.* **2017**, *8*, 3720–3725.

32. Saidi, W. A.; Poncé, S.; Monserrat, B. Temperature Dependence of the Energy Levels of Methylammonium Lead Iodide Perovskite from First-Principles. *J. Phys. Chem. Lett.* **2016**, *7*, 5247–5252.

33. Boyer-Richard, S.; Katan, C.; Traoré, B.; Scholz, R.; Jancu, J.-M.; Even, J. Symmetry-Based Tight Binding Modeling of Halide Perovskite Semiconductors. *J. Phys. Chem. Lett.* **2016**, *7*, 3833–3840.

34. Møller, C. K. The Structure of Perovskite-like Caesium Plumbo Trihalides. *Mat. Fys. Medd. Dan. Vid. Sels.* **1959**, *32, No 2*.

35. Trots, D. M.; Myagkota, S. V.; Voloshinovskii, A. S. Crystal Structure and Thermal Expansion of $CsPbBr_3$ in the range of 12-300K. 2009; `http://photon-science.desy.de/annual_report/files/2009/2009612.pdf`.

36. Stoumpos, C. C.; Malliakas, C. D.; Peters, J. A.; Liu, Z.; Sebastian, M.; Im, J.; Chasapis, T. C.; Wibowo, A. C.; Chung, D. Y.; Freeman, A. J.; Wessels, B. W.; Kanatzidis, M. G. Crystal Growth of the Perovskite Semiconductor $CsPbBr_3$: A New Material for High-Energy Radiation Detection. *Cryst. Growth Des.* **2013**, *13*, 2722–2727.

37. Mori, M.; Saito, H. An X-ray Study of Successive Phase Transitions in $CsSnBr_3$. *J. Phys. C* **1986**, *19*, 2391.

38. Fabini, D. H.; Laurita, G.; Bechtel, J. S.; Stoumpos, C. C.; Evans, H. A.; Kontos, A. G.; Raptis, Y. S.; Falaras, P.; Van der Ven, A.; Kanatzidis, M. G.; Seshadri, R. Dynamic Stereochemical Activity of the Sn^{2+} Lone Pair in Perovskite $CsSnBr_3$. *J. Am. Chem. Soc.* **2016**, *138*, 11820–11832.

39. Kontos, A. G.; Kaltzoglou, A.; Afranis, M.; McCall, K. M.; Stoumpos, C. C.; Kanatzidis, M.; Falaras, P. Bandgap Widening and Persistent Near-IR Photoluminescence at High Temperature in $ASnI_3$ Perovskites (A = Cs^+, $CH_3NH_3^+$ and $NH_2{-}CH = NH_2^+$). *Manuscript in preparation*

40. Božin, E. S.; Malliakas, C. D.; Souvatzis, P.; Proffen, T.; Spaldin, N. A.; Kanatzidis, M. G.; Billinge, S. J. L. Entropically Stabilized Local Dipole Formation in Lead Chalcogenides. *Science* **2010**, *330*, 1660–1663.

41. Laurita, G.; Fabini, D. H.; Stoumpos, C. C.; Kanatzidis, M. G.; Seshadri, R. Chemical Tuning of Dynamic Cation off-centering in the Cubic Phases of Hybrid Tin and Lead Halide Perovskites. *Chem. Sci.* **2017**, *8*, 5628–5635.

42. Pedesseau, L.; Sapori, D.; Traoré, B.; Robles, R.; Fang, H.-H.; Loi, M. A.; Tsai, H.; Nie, W.; Blancon, J.-C.; Neukirch, A.; Tretiak, S.; Mohite, A. D.; Katan, C.; Even, J.; Kepenekian, M. Advances and Promises of Layered Halide Hybrid Perovskite Semiconductors. *ACS Nano* **2016**, *10*, 9776–9786.

43. Even, J.; Carignano, M.; Katan, C. Molecular Disorder and Translation/Rotation Coupling in the Plastic Crystal Phase of Hybrid Perovskites. *Nanoscale* **2016**, *8*, 6222–6236.

44. Létoublon, A.; Paofai, S.; Rufflé, B.; Bourges, P.; Hehlen, B.; Michel, T.; Ecolivet, C.; Durand, O.; Cordier, S.; Katan, C.; Even, J. Elastic Constants, Optical Phonons, and Molecular Relaxations in the High Temperature Plastic Phase of the $CH_3NH_3PbBr_3$ Hybrid Perovskite. *J. Phys. Chem. Lett.* **2016**, *7*, 3776–3784.

45. Cowley, R. Structural Phase Transitions I. Landau Theory. *Adv. Phys.* **1980**, *29*, 1–110.

46. Rousseau, B.; Bergara, A. Giant Anharmonicity Suppresses Superconductivity in AlH_3 under Pressure. *Phys. Rev. B* **2010**, *82*, 104504.

47. Baroni, S.; de Gironcoli, S.; Dal Corso, A.; Giannozzi, P. Phonons and Related Crystal Properties from Density-Functional Perturbation Theory. *Rev. Mod. Phys.* **2001**, *73*, 515–562.

48. Burfoot, J. C., Entropy of an Order-Disorder Transition. *J. Phys., Colloq.* **1972**, *33*, C2–79–C2–81, Colloque C2.

49. Harrison, J. W.; Hauser, J. R. Theoretical Calculations of Electron Mobility in Ternary III-V Compounds. *J. Appl. Phys.* **1976**, *47*, 292–300.

50. Slater, J. C.; Koster, G. F. Simplified LCAO Method for the Periodic Potential Problem. *Phys. Rev.* **1954**, *94*, 1498–1524.

51. Eperon, G. E.; Stranks, S. D.; Menelaou, C.; Johnston, M. B.; Herz, L. M.; Snaith, H. J. Formamidinium Lead Trihalide: a Broadly Tunable Perovskite for Efficient Planar Heterojunction Solar Cells. *Energy Environ. Sci.* **2014**, *7*, 982.

52. Katan, C.; Pedesseau, L.; Kepenekian, M.; Rolland, A.; Even, J. Interplay of Spin-orbit Coupling and Lattice Distortion in Metal Substituted 3D Tri-chloride Hybrid Perovskites. *J. Mater. Chem. A* **2015**, *3*, 9232–9240.

53. Even, J.; Pedesseau, L.; Jancu, J.-M.; Katan, C. DFT and k·p Modelling of the Phase Transitions of Lead and Tin Halide Perovskites for Photovoltaic Cells. *Phys. Status Solidi RRL* **2014**, *8*, 31–35.

54. Even, J.; Pedesseau, L.; Jancu, J.-M.; Katan, C. Importance of Spin–Orbit Coupling in Hybrid Organic/Inorganic Perovskites for Photovoltaic Applications. *J. Phys. Chem. Lett.* **2013**, *4*, 2999–3005.

55. Marronnier, A.; Lee, H.; Lee, H.; Kim, M.; Eypert, C.; Gaston, J.-P.; Roma, G.; Tondelier, D.; Geffroy, B.; Bonnassieux, Y. Electrical and Optical Degradation Study of Methylammonium-based Perovskite Materials under Ambient Conditions. *Sol. Energy Mater. Sol. Cells* **2018**, *178*, 179 – 185.

56. Lee, P. L.; Shu, D.; Ramanathan, M.; Preissner, C.; Wang, J.; Beno, M. A.; Von Dreele, R. B.; Ribaud, L.; Kurtz, C.; Antao, S. M.; Jiao, X.; Toby, B. H. A Twelve-analyzer Detector System for High-resolution Powder Diffraction. *J. Synchrotron Radiat.* **2008**, *15*, 427–432.

57. Dalesio, L. R.; Hill, J. O.; Kraimer, M.; Lewis, S.; Murray, D.; Hunt, S.; Watson, W.; Clausen, M.; Dalesio, J. *Nucl. Instrum. Methods Phys. Res., Sect. A* **1994**, *352*, 179.

58. Petříček, V.; Dušek, M.; Palatinus, L. Crystallographic Computing System JANA2006: General features. *Z. Kristallogr. - Crist. Mater.* **2014**, *229*.

59. Woodward, P. M. Octahedral Tilting in Perovskites. I. Geometrical Considerations. *Acta Crystallogr. B* **1997**, *53*, 32–43.

60. Hohenberg, P.; Kohn, W. Inhomogeneous Electron Gas. *Phys. Rev.* **1964**, *136*, B864–B871.

61. Kohn, W.; Sham, L. J. Self-Consistent Equations Including Exchange and Correlation Effects. *Phys. Rev.* **1965**, *140*, A1133–A1138.

62. Giannozzi, P.; Baroni, S.; Bonini, N.; Calandra, M.; Car, R.; Cavazzoni, C.; Ceresoli, D.; Chiarotti, G. L.; Cococcioni, M.; Dabo, I.; Corso, A. D.; de Gironcoli, S.; Fabris, S.; Fratesi, G.; Gebauer, R.; Gerstmann, U.; Gougoussis, C.; Kokalj, A.; Lazzeri, M.; Martin-Samos, L. *et al.* Quantum Espresso: a Modular and Open-source Software Project for Quantum Simulations of Materials. *J. Phys.: Condens. Matter* **2009**, *21*, 395502.

63. Monkhorst, H. J.; Pack, J. D. Special Points for Brillouin-zone Integrations. *Phys. Rev. B* **1976**, *13*, 5188–5192.

64. Kresse, G.; Furthmüller, J. Efficient Iterative Schemes for Ab Initio Total-energy Calculations using a Plane-wave Basis Set. *Phys. Rev. B* **1996**, *54*, 11169–11186.

65. Kresse, G.; Furthmüller, J. Efficiency of Ab-initio Total Energy Calculations for Metals and Semiconductors using a Plane-wave Basis set. *Comput. Mater. Sci.* **1996**, *6*, 15 – 50.

66. Shishkin, M.; Kresse, G. Implementation and Performance of the Frequency-dependent *GW* Method within the PAW Framework. *Phys. Rev. B* **2006**, *74*, 035101.

67. Perdew, J. P.; Burke, K.; Ernzerhof, M. Generalized Gradient Approximation Made Simple. *Phys. Rev. Lett.* **1996**, *77*, 3865–3868.

68. Perdew, J. P.; Burke, K.; Ernzerhof, M. Generalized Gradient Approximation Made Simple [Phys. Rev. Lett. 77, 3865 (1996)]. *Phys. Rev. Lett.* **1997**, *78*, 1396–1396.

69. Steiner, S.; Khmelevskyi, S.; Marsmann, M.; Kresse, G. Calculation of the Magnetic Anisotropy with Projected-augmented-wave Methodology and the Case Study of Disordered $Fe_{1-x}Co_x$ Alloys. *Phys. Rev. B* **2016**, *93*, 224425.

70. Hedin, L. New Method for Calculating the One-Particle Green's Function with Application to the Electron-Gas Problem. *Phys. Rev.* **1965**, *139*, A796–A823.

71. van Schilfgaarde, M.; Kotani, T.; Faleev, S. Quasiparticle Self-Consistent *GW* Theory. *Phys. Rev. Lett.* **2006**, *96*, 226402.

72. Shishkin, M.; Kresse, G. Self-consistent *GW* Calculations for Semiconductors and Insulators. *Phys. Rev. B* **2007**, *75*, 235102.

73. Fuchs, F.; Furthmüller, J.; Bechstedt, F.; Shishkin, M.; Kresse, G. Quasiparticle Band Structure Based on a Generalized Kohn-Sham Scheme. *Phys. Rev. B* **2007**, *76*, 115109.

74. Shishkin, M.; Marsman, M.; Kresse, G. Accurate Quasiparticle Spectra from Self-Consistent GW Calculations with Vertex Corrections. *Phys. Rev. Lett.* **2007**, *99*, 246403.

75. Pack, J. D.; Monkhorst, H. J. "Special Points for Brillouin-zone Integrations"—a reply. *Phys. Rev. B* **1977**, *16*, 1748–1749.

Graphical TOC Entry